Technische Universität Berlin

AG Wagner

Bachelor Thesis

Depth-resolved Raman spectroscopy of InN and GaN

Fabian Heisinger

supervised by
Dr. Maximilian Ries

reviewer:
Dr. Markus Wagner
Dr. Andrei Schliwa

February 1, 2022

Name ....

geb. ....

Matr. Nr: ....

WS 2021/22

Erklärung/Statutory Declaration

Hiermit erkläre ich, dass ich die Bachelor-Arbeit selbstständig verfasst, noch nicht anderweitig für Prüfungszwecke vorgelegt, keine anderen als die angegebenen Quellen oder Hilfsmittel benutzt sowie wörtliche und sinngemäße Zitate als solche gekennzeichnet habe.

I declare that I have authored this thesis independently, that I have not used other than the declared sources/resources, and that I have explicitly marked all material, which has been quoted either literally or by content from the used sources.

....

Ort, Datum   Unterschrift

Contents

1   Introduction

Semiconductors and the corresponding electrical devices like the LED[1–8] (light emitting diode) or transistor[1, 9–11], have become an essential part of daily life: from LEDs replacing light bulbs, to LED-based television and computer screens, from lasers[3] for reading optical stored data in CDs, and data transport via fiber optic cable, to transistors being the key component in logic gates[1, 10] that again are used to create microprocessors for computers.

The variety of applications is based on the intrinsic properties of semiconductors, like the energy band gap, the electrical conductivity, and the build-in potential. While metals can conduct electricity at any time due to partially filled energy bands, insulators and semiconductors can not because they have only empty bands. The differences between insulators and semiconductors is based on the size of the energy band gap. If the band gap is small enough for energy states of the conduction band to be occupied at room temperature, these materials are called semiconductors. This implies an increased electrical conductivity owing to thermally excited electrons based on the widening of the Fermi-function with temperature. Contrary, insulators do not show electrical conductivity at room temperature[12].

The band gap energy can be influenced by doping, i.e. by the deliberate inclusion of other atoms from neighboring groups in the periodic table. Due to the differing amount of valence electrons of the doped material compared to the semiconductor, holes or loosely bound electrons occur based on the type of doping in the material. The doped semiconductors are named with the prefix "n" if they have loosely bound electrons or "p" if they contain holes. This eneases thermal excitation of electrons for n-doped semiconductors and increases the conduction for both kinds.

By bringing a p- and an n-type semiconductor in contact, a so-called p-n junction[1, 3, 4], the loosely bound conduction band electrons will fill the respected holes. Consequently, an electrical field emerges due to the ionised doped atom cores on the n-side and extra electrons on the p-side. This build-in potential can be influenced by a current applied on the junction, in p-n-p junctions this can be used to control the flow of electric current and is the fundamental working principle of transistors[1, 3, 9]. If radiation is absorbed in the region of the build-in potential, the exited electron is diverted by the electric field. This leads to carrier separation and is exploited in solar panels[13].

A popular example for semiconducting materials is silicon (Si), because its relative cheap production cost and natural abundance it is a common choice for solar panels[14, 15]. Binary semiconductors like GaN, with its wide range of applications in detectors, lasers, amplifiers and lighting[6, 11], as well as its ternary and quaternary combinations with AlN, InN have become key materials[7, 8] due to the wide range of band bap energies (0.7 eV for InN to 3.4 eV for GaN to 6 eV for AlN[16]) they cover[17].

The high melting temperature of nitrides makes standard crystallization techniques not applicable. Nitrides have to be grown heteroepitaxially, i.e. on foreign substrates (such as sapphire)[18–20]. Due to the differences in crystal structure, lattice parameters, and thermal expansion coefficients, structural imperfections like defects and dislocations as well as stress and strain emerge in heteroepitaxy.

In this work, InN and GaN are examined. Depth-resolved confocal Raman spectroscopy is applied to investigate carrier accumulations on surfaces as well as the change of the Raman frequency with depth to gain information on the internal material stress.

In the following section 2 is the general theoretical ground described. InN is examined in section 4 while the experiments on GaN, which will be published in a paper, are included in section 6. Both sections present applied evaluation and methods.

The developed Python codes and measurement data are uploaded to Github, see `https://github.com/FHeisinger/Bachelorarbeit`.

2 Theoretical background

2.1 Crystal structure

Group-III-Nitrides exist thermodynamically stable in wurtzite (Wz) structure under ambient conditions and can be expressed in space groups as $P6_3mc$ in Hermann-Mauguin or $C_{6\nu}^4$ in Schönfließ notation. They can be stabilized furthermore in zinc blend (ZB) structure on cubic substrates and under constant high pressures also in rock salt form[17].

The Wz structure contains two atom pairs in its primitive cell, where every atom is surrounded tetrahedrally by four atoms of the other kind. The stacking order is ABAB..., where every sublayer A and B is ideally comprised of closed packed layers of spheres. It has a hexagonal base with side length a and an overall height c, as shown in figure 1a, defining the lateral and in-plane distances.

Crystallographic planes are described by the Miller indices. These are the inverse intersection lengths of planes with the coordinate system axis of the crystal and to integers reduced. In case of Wz there are four axes, three describing the hexagonal base area $\bar{a}_1, \bar{a}_2, \bar{a}_3$ and one describing the height $\bar{c}$. In figure 1b the axis are shown alongside the r-, c-, m-, and a-plane with their respective Miller indices[12].

In reciprocal space the lattice can also be described by a number of points and the connections between them. This becomes handy to describe diffraction inperiodic structures and energy relations. The center of the lattice is called Γ point.

Group theory predicts eight phonon modes, two acoustic and six optical, at the Γ point. The optical modes are depicted in figure 2. A_1 and B_1 have atomic displacements along the $\bar{c}$ axes (see figures 2d, 2e, 2f), while E_1 and E_2 (figures 2a, 2b, 2c) oscillate perpendicular to it. The A_1 and E_1 modes are Raman and infrared active, while the E_2(high) and E_2(low) are only Raman active, and the B_1(high) and B_1(low) are silent[21].

(a)

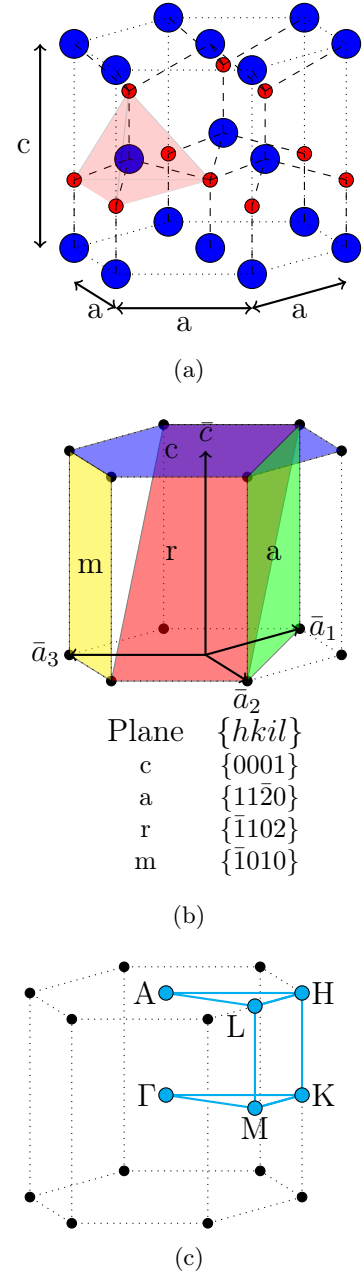| Plane	$\{hkil\}$
c	$\{0001\}$
a	$\{11\bar{2}0\}$
r	$\{\bar{1}102\}$
m	$\{\bar{1}010\}$

(b)

(c)

Figure 1: Atomic placement of the two kinds of atoms in Wz structure, distaces c and a in (a). Basic planes of Wz in (b) with respective notation. Reciprocal lattice points in Wz (c).
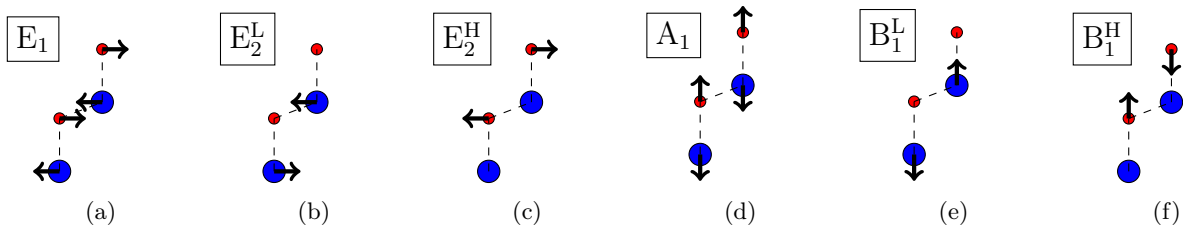

(a)   (b)   (c)   (d)   (e)   (f)

Figure 2: Wz optical phonon modes and their direction of atomic oscillation[21]

2

2.2 Raman spectroscopy

Raman spectroscopy is a widely used optical spectroscopy technique to study the vibrational properties of materials by utilising the inelastic scattering of light by molecular vibrations[22].

It is named after Sir Chandrasekhara Venkata Raman for the discovery of the effect and was awarded with the Nobel Prize in 1930 [23–25]. It is a useful tool for analyzing semiconductors, especially hetero-structures and interfaces. It provides information on lattice dynamics and electronic properties, which allow for material identification as well as knowledge of composition of compounds, layer orientation, stress and the crystalline perfection of the material in question[26].

In an idealized medium (i.e. infinite volume and perfect periodic structure), the polarization $\mathbf{P}(\mathbf{k}, \omega)$ can be expressed as the product of the susceptibility χ and the electric field $\mathbf{E}(\mathbf{r}, t)$. Considering an electric field with sinusodial change

$$\mathbf{E}(\mathbf{r}, t) = \mathbf{E}(\mathbf{k}, \omega) \cos\left(\mathbf{k} \cdot \mathbf{r} - \omega t\right) \tag{1}$$

this would induce a polarization

$$\mathbf{P}(\mathbf{r}, t) = \epsilon_0 \chi(\mathbf{k}, \omega) \mathbf{E}(\mathbf{r}, t) \tag{2}$$

$$\mathbf{P}(\mathbf{r}, t) = \mathbf{R}(\mathbf{k}, \omega) \cos\left(\mathbf{k} \cdot \mathbf{r} - \omega t\right) \tag{3}$$

inside the medium[22].

If now the atomic displacement $\mathbf{Q}(\mathbf{r}, t)$, associated with phonons, are considered as plane waves like

$$\mathbf{Q}(\mathbf{r}, t) = \mathbf{Q}(\mathbf{q}, \omega_q) \cos\left(\mathbf{q} \cdot \mathbf{r} - \omega_q t\right) \tag{4}$$

it can be shown[22] that χ can change due to these vibrations like

$$\chi(\mathbf{k}, \omega, \mathbf{Q}) = \chi_0(\mathbf{k}, \omega) + \left(\frac{\partial \chi}{\partial \mathbf{Q}}\right)_0 \mathbf{Q}(\mathbf{r}, t) \tag{5}$$

This is nothing other than the first order of Taylor approximation of χ.

With this expression, the equation (2) can be written as

$$\mathbf{P}(\mathbf{r}, t, \mathbf{Q}) = \mathbf{P}_0(\mathbf{r}, t) + \mathbf{P}_{ind}(\mathbf{r}, t, \mathbf{Q}) \tag{6}$$

$$\mathbf{P}_0(\mathbf{r}, t) = \chi_0(k, \omega) \mathbf{E}(\mathbf{k}, \omega) \cos\left(\mathbf{k} - \mathbf{r} - \omega t\right) \tag{7}$$

$$\mathbf{P}_{ind}(\mathbf{r}, t, \mathbf{Q}) = \left(\frac{\partial \chi}{\partial \mathbf{Q}}\right)_0 \mathbf{Q}(\mathbf{r}, t) \mathbf{E}(\mathbf{k}, \omega) \cos\left(\mathbf{k} \cdot \mathbf{r} - \omega t\right) \tag{8}$$

where $\mathbf{P}_0(\mathbf{r}, t)$ describes the polarization in phase with the electric field and $\mathbf{P}_{ind}(\mathbf{r}, t, \mathbf{Q})$ the one induced by the phonon[22]. Furthermore, it can be written, using a cosine identity while incorporateing equation (4), as:

$$\begin{aligned} \mathbf{P}_{ind}(\mathbf{r}, t, \mathbf{Q}) = &\frac{1}{2} \left(\frac{\partial \chi}{\partial \mathbf{Q}}\right)_0 \mathbf{Q}(\mathbf{q}, \omega_q) \mathbf{E}(\mathbf{k}, \omega) \\ &\times \left\{\cos\left[(\mathbf{k} + \mathbf{q})\mathbf{r} - (\omega + \omega_q)\right] + \cos\left[(\mathbf{k} - \mathbf{q})\mathbf{r} - (\omega - \omega_q)\right]\right\} \end{aligned} \tag{9}$$

This equation describes the polarisation by the atomic displacement $\mathbf{Q}$, and the interaction of the electric and phonon frequencies. The first part with wave vector $\mathbf{k}_{AS} = \mathbf{k} + \mathbf{q}$ and frequency $\omega_{AS} = \omega + \omega_q$ is named anti-Stokes and the associated radiation the anti-Stokes scattered light. Wave vector $\mathbf{k}_S = \mathbf{k} - \mathbf{q}$ and frequency $\omega_A = \omega - \omega_q$ are the Stokes and the Stokes scattered light. The difference between the incident photon and the scattered one is named the Raman frequency[22].

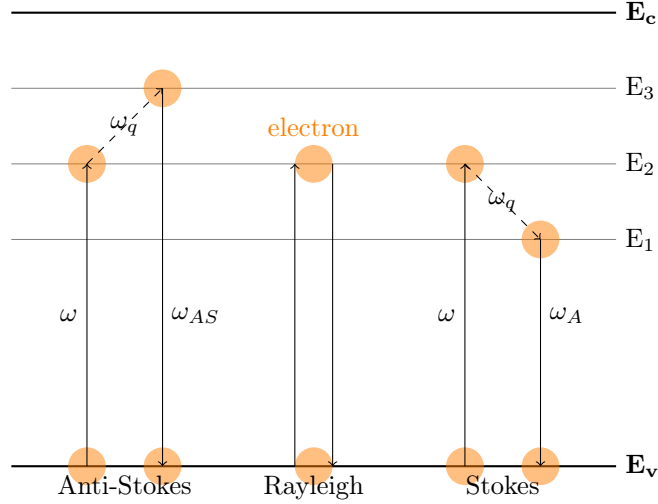A schematic visualization can be seen in figure 3.

Figure 3: Schematic of Raman scattering in an energy diagram. $\mathbf{E_v}$ represents the valence band energy and $\mathbf{E_c}$ the conduction band energy. E_1, E_2 and E_3 are intermediate states, where the inelastic scattering occurs. ω refers to the incoming light, while ω_{AS} and ω_S are the anti-Stokes scattered and Stokes scattered light, respectively. ω_q refers to the phonon frequency.

It is important to notice that the frequency and wave-vector are conserved! Hence, the selection rules can be written as:

- wave vector:

$$k_i = k_{out} \pm q \tag{10}$$

- frequency:

$$\omega_i = \omega_{out} \pm \omega_q \tag{11}$$

Furthermore, it is possible to use a higher order of approximation for the atomic displacement, resulting in more possibilities for shifted frequencies. While the described approximation gives the one-phonon Raman scattering, higher orders describe multiple-phonon Raman scattering (e.g. two-phonon Raman scattering)[22].

Confocal Raman spectroscopy

One way of measuring the Raman effect is confocal Raman spectroscopy, whereby an optical microscope is coupled to a Raman spectrometer. As a result, the high magnification and spatial filtering in lateral (x,y) and axial (z) directions of the microscope to obtain volume specific spectral information[27, 28].

The parallel laser light is is first widened by a set of lenses to illuminate the objective fully and than focused onto the sample. Reflected light from the focus area is gathered by the objective and directed to the confocal microscope, consisting of two lenses and a pinhole. The light is focused through the pinhole, which acts as a spatial filter that only allows light in an area around the focal plane to pass. The area can be adjusted by the pinhole size. The light is parallelized by the second lens and ultimately focused into the spectrometer via an entrance slit[29].

Limitations of this method are the small investigated volumes, restricting from bulk analysis if the sample is not homogeneous, and long measurement times. Thus, areas under investigation need to be representative of the entire sample[29]. Furthermore, when investigating changes in depth (axial (z) direction) over interfaces (like air-sample), the refraction index mismatch has to be taken into account[30].

2.3 Light refraction at interfaces

Light, when reaching a planar interface, refracts based on the refraction indexes of the materials on either side of the interface. Because of this, data collected through an interface, needs to be corrected by the occurring change in light angle and with this focus distance. Baldwin and Batchelder[31] describe this effect with a general refraction index n

$$n = \frac{n_2}{n_1},$$
(12)

were n_2 denotes the material containing the focus point and n_1 in this case containing the lens. The numerical aperture NA of the objective lens is given by

$$\text{NA} = \sin\theta_{max},$$
(13)

and θ_{max} is the maximum angle at which the light can be focused onto the focus point. It is possible that the light does not fully fill the entire lens radius r_{max}. So, the fractional height m of a ray in the lens is introduced. The actual radius r the light takes as well as the angle θ_{max}, are shown in figure 4.

$$m = \frac{r}{r_{max}}$$
(14)

Figure 4: Visualization of the geometry and parameters during refraction. Note the two radii denoting the actual width r and the maximum width r_{max} of the light beam entering the objective lens. θ_{max} denotes the maximum focus angle, θ_0 the beam angle without refraction focused at P_0 with distance z_0, and θ the angle under refraction focused at P with distance z. Inspired by[31]

The actual focus point inside the new material can then be expressed as a function of the unrefracted measured from the perspective of n_1 as

$$z = Mnz_0$$
(15)

with the quantity M[31]

$$M = \sqrt{1 + \frac{m^2 \text{NA}^2 (n^2 - 1)}{(1 - \text{NA}^2) n^2}}$$
(16)

With this, a theoretical depth compression factor of $\frac{z}{z_0}$ can be calculated and used to correct the depth scale inside the material in question. Chen and Lu have shown the practicability of this in their work on GaN diode structures[30].
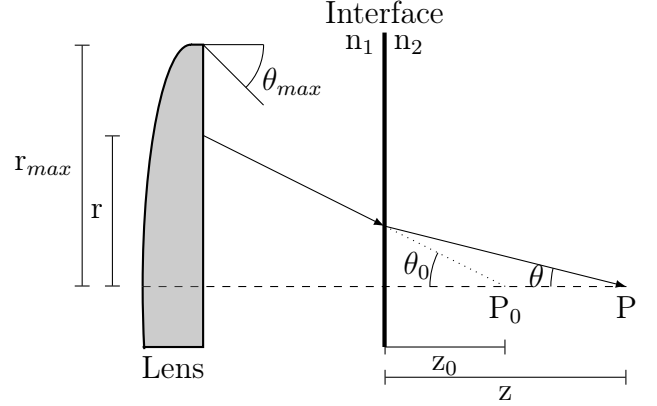
2.4 Strain and stress

The effect of a force per unit area that acts on the face of an elementary cube in a material is called stress. As a result the position of the atoms in the material are altered in the direction of the force and the chemical bond lengths are changed. Mathematically, stress is described by the stress tensor σ. If the force points towards the unit cell center, the stress is called compressive, while tensile stress refers to an outwards pointing force[22]. Stress in semiconductor heterostructures arises mainly from differences in the thermal expansion coefficient between materials during cooling of the sample after the growth process[32]. Owing to the high thermal stability of semiconducting materials, the growth processes involve high temperatures that lead to large temperature differences during cooling.[22] Furthermore, tensile stress is created if the initial growth consists of small crystallites that ultimately grow together at coalescence boundaries, as is the case by GaN[32]. Another source of stress is doping. As the incorporated doping material is different from the layer material, stress is induced depending on the respected materials.

Furthermore, the change between different stress states is described by the strain ϵ. In general, stress and strain relate though the fourth-rank tensors of the elastic compliance S and elastic stiffness C[22, 32]:

$$\epsilon = S\sigma \qquad \text{and} \qquad \sigma = C\epsilon. \qquad (17)$$

In case of in-plane stress, it is also possible to calculate the in-plane strain via the in-plane biaxial modulus M_f[32]:

$$M_f = \frac{E}{1-\nu} \qquad \text{, so that} \qquad \sigma_f = M_f\epsilon_m. \qquad (18)$$

Here E is the Young's modulus and ν the Poisson ration. Both are calculated from the independent elastic constants of the respected materials.

Stress can be observed *in situ* by optical reflection methods, due to the bending moment being exerted on the substrate by the growing film. In equilibrium, this bending is equal for substrate and film[32]. It can be measured as the so called curcature κ. This curvature can be described by the mismatch strain ϵ_m, the biaxial moduli $M_{s,f}$ of the substrate s and the film f, as well as thicknesses $h_{s,f}$ via the Stoney Equation[32, 33]:

$$\kappa = \frac{6m\epsilon_m h_f}{h_s^2} \qquad \text{, with} \qquad m = \frac{M_f}{M_s}. \qquad (19)$$

Due to the effects of stress on the atomic structure, the vibrational properties are influenced, which can be measured by Raman spectroscopy. In general, tensile stress causes a shift of the Raman frequencies towards lower values while compressive stress results in a shift towards higher frequency values[16, 34]. Furthermore, it is possible to calculate the shifted frequency ω_{shift}, if the raman frequency ω_0 of the phonon mode in a unstressed case, as well as the change in frequency per applied pressure $\frac{\partial \omega}{\partial P}$ for the hydraulic pressure P in known:

$$\omega_{shift} = \omega_0 + \frac{\partial \omega}{\partial P}P \qquad (20)$$

These parameters can be gathered experimentally, as has been done by Reparaz et al. for InN [35].
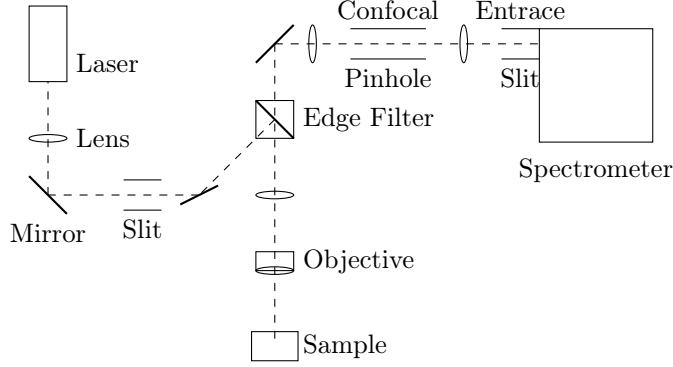
3   Experimental setup

Figure 5: Schematic of the experimental setup. The laser beam is widened by a set of lenses. An edge filter guides the light through the objective. The back-scattered beam is wavelength-filtered by the edge filter and spatially filtered by the confocal pinhole. The remaining light enters the spectrometer via an entrance slit.

A 532 nm external laser was used in a HORIBA HR800 integrated Raman system. An x100 MPlan N objective with an numeric aperture of NA = 0.9 is installed in the pre-included microscope.

The laser beam is widened by a set of lenses between the laser and objective to iluminate the objective fully. These lenses are designed for the integrated 633 nm laser and do not function properly for other wavelengths, i.e., the beam is not widened perfectly. The beam is guided by mirrors through a first slit onto the edge filter.

The edge filter acts as a semi-transparent mirror and reflects the beam through the second lens, parallelizing the light. Subsequently, the beam is focused by the objective onto the sample. The measurements are taken in $(z)(-,-)(\bar{z})$ backscattering geometry. Then, the reflected radiation is wavelength-filtered by the edge filter. A second set of lenses widens the beam in order to spatially filter it by the confocal pinhole. Light that does not originate from the focal plane is not fully parallel. Consequently, widening the beam and focusing it through a hole will result in imperfectly parallel radiation to be defocused at the hole. Effectively, large parts are not passing through the confocal pinhole, see figure 6. Finally, the beam is focused onto the entrance slit of the spectrometer. There, the beam is diffracted via a grating. In case of the InN measurements, a grating with 1800 lines per mm has been used. The signal is recorded with a Syncerity CCD camera.

For the depth-resolved measurements, the objective is moved along the z-axes in 100 nm steps and Raman spectra are recorded at each step. This process is automated by the setup software.
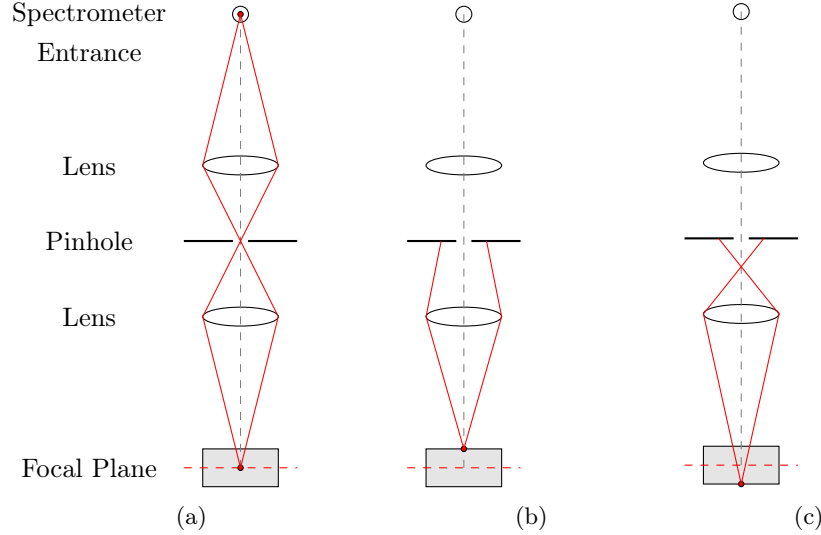

Figure 6: Schematic of a confocal pinhole. (a) The light from the focal plane passes through the pinhole. (b) and (c) show that light originating from above and below the focal plane is predominantly blocked because it will be not be focused onto the pinhole by the lens.

4 Depth-resolved Raman spectroscopy of InN

This chapter presents depth-resolved Raman spectroscopy of InN samples. The following pages will describe how vibrational information changes over the sample depth by moving the lens focus and will discuss the consequences that arise.

InN was a main focus of semiconductor research in the last two decades, following the discovery of the surprisingly narrow band gap[36], but interest has decreased due to the still difficult growth process. The main reason for this work is the discovery of additional modes in InN with tip-enhanced Raman spectroscopy (TERS). The results obtained by Poliani, Ries et al.[37–39] suggest an explanation by an accumulation of charges at the interfaces. To check this theory, depth-resolved Raman spectroscopy is employed to find possible evidence in the behavior of the polar (A_1, E_1) and non-polar (E_2(high)) optical phonon modes. Because, polar phonons create an macroscopic electric field, they change under carrier accumulation[40]. Making the ratio of the polar and non-polar modes a indicator for carrier accumulation.

The investigated materials are one a-plane and two c-plane-orientated hexagonal InN samples. These are grown by molecular beam epitaxy (MBE), migration-enhanced plasma-assisted MOCVD (MEPA-MOCVD) and metal-organic chemical vapor deposition (MOCVD). The different bulk sizes and other parameters are listed in table 1.
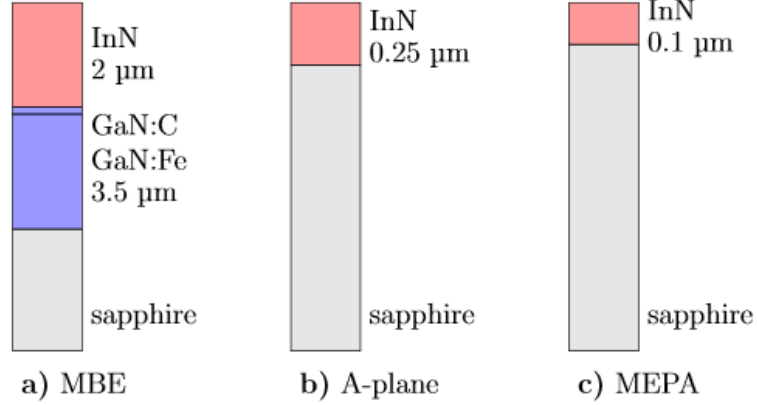

Figure 7: Visualization of the sample structure and the InN layer thickness.

InN	d	sub	buf	n_e
	in μm		in μm	cm^{-1}
c-MBE	2	Al_2O_3	0.1 GaN:C	5.2×10^{17}
			3.5 GaN:Fe	
a-MOCVD	0.25	Al_2O_3		8×10^{19}
c-MEPA	0.1	Al_2O_3		1×10^{19}

Table 1: Thicknesses d of InN/GaN layer, substrates (sub), buffer layer (bu), and n_e carrier concentration n_e of the InN samples. Values from [39].

The measurements are taken in $(z)(-,-)(\bar{z})$ backscattering geometry for the InN c-plane samples and in $(x)(-,-)(\bar{x})$ for the InN a-plane. The spectra analysis is accomplished via Python code to automatically fit the phonon modes in the Raman data for very depth. The inaccuracy of the fits can be estimated via the residuals of the fitted functions and are in the realm of up to 5%.

4.1 InN MBE

The MBE sample is a 2 μm c-plane InN layer on c-plane GaN upon sapphire substrate. In back scattering, the modes E_2 and $A_1(LO)$ Modes are expected[21]. A representative spectrum is shown in fig 8. Observable modes are the E_2(high) and $A_1(LO)$ mode of InN, found at 493 and 595 cm^{-1}, as well as the GaN E_2 mode at 570 cm^{-1}. These frequencies match well with the reported frequencies by Davydov[41] and Harima[21], see table 2.

The data background is estimated by fitting a 5th degree polynomial and subtracted from the measurement. Fitting is automated for all spectra via Python code and spectra from different depths are shown in the appendix.

Figure 8: Exemplary Raman spectrum of the MBE sample.

The intensities of the fitted Raman peaks as a function of depth, or rather the distance the lens moved in z-direction are shown in figure 9. Since the light beneath the InN air interface is refracted by the interface, the measurements are depth-corrected by a compression factor $\frac{z}{z_0}$ of 3.08. z is the actual and z_0 the measured depth by the movement of the piezoelectric z-stage[30, 31]. The refraction index of InN is $n_{InN}=2.6$[42]. Only the air/InN refraction has been corrected. Due to missing information, a fraction height of $m = \frac{1}{2}$ was assumed , i.e., the beam radius of the laser is half the radius of the objective lens. All negative position values in the following figures are multiplied by the depth compression factor to account for the mismatch.
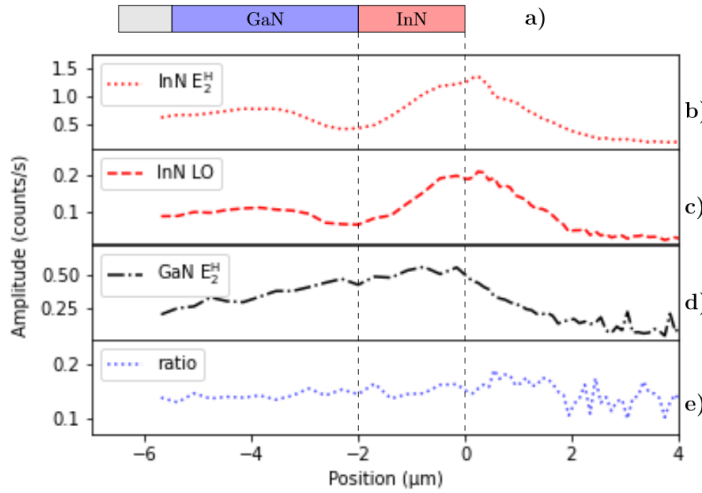

Figure 9: Fitted intensities of the Raman modes plotted in relation to the corrected depth of the focus, with sample structure in (a) as reference for the MBE sample. InN E_2(high) in (b) and the LO in (c), their ratio in (e). (d) GaN E_2(high).

The air/sample interface is set to $x = 0$ and has been picked by taking the frequency shift into account, see figure 10. The frequency exhibits a noticeable minimum in its depth-dependence. That is explained by stress relaxation and subsequent frequency lowering. The interface is set to the end of the minimum plateau, because it can be argued that the minimal stress is near the air/InN interface. Detailed argumentation regarding the Raman modes frequency shift is presented after the following analysis of the Raman modes amplitudes and FWHMs:

Negative notated position are located inside the sample, judging from the behaviour of the GaN E_2(high) mode (figure 9d). Which begins rising, has its maximum around position -1.5, and then falls off with a FWHM of 6 μm. The InN modes (figure 9a and b) exhibit an unexpected behaviour with two maxima. One above the GaN E_2(high) peak maximum, originating most likely from the InN layer with the maximum at position -0.5 and an estimated FWHM of 2.5 μm, close to the expected layer width, see table 1. The second maximum, deeper inside the sample, occurs around position -4. A possible explanation could be reflection at the InN/GaN interface. The InN LO mode exhibits the same behavior as the E_2(high).
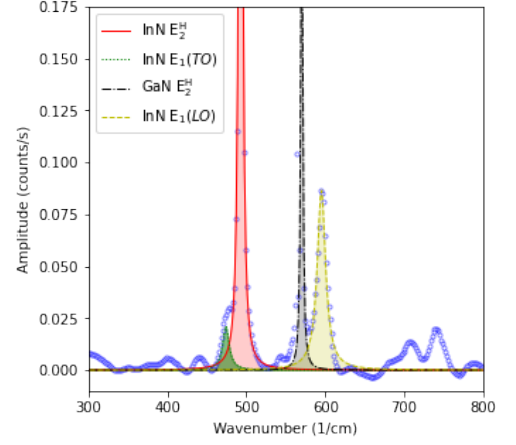
9

material	mode	Davydov[41]	Harima[21]
		cm^{-1}	
InN	E$_2$(high)	491.5	488
	A$_1$(LO)	580.5	586
	E$_1$(LO)	591	593
GaN	E$_2$(high)		568

Table 2: Raman frequencies for InN and GaN, from [21, 41]

The ratio of LO and E$_2$(high) (figure 9e) shows a small rising trend towards the sample surface, before reaching its maximum shortly after the main maximum of the E$_2$(high). This ratio is used to show the influence of carrier accumulation on the LO mode. Which is a longitudinal and polar vibration creating a macroscopic electric field. This field can interact with the carriers, resulting in a broadening and an intensity increase of the Raman mode for higher carrier accumulation[43, 44]. A increase in the ratio suggests therefore a accumulation of carriers. This suggests a carrier accumulation on the air/InN interface, but is because of low intensity not reliable.

The FWHM of the fitting functions (fig 22 in attachment) exhibits a fluctuating behaviour. For the LO mode, this could be caused by the low intensity of this peak challenging the fitting algorithm, or is a result of broadening by carrier accumulation[43, 44]. The InN E$_2$(high) FWHM shows a noticeable maximum slightly deeper in the sample, than the amplitude maximum. Given that the FWHM can be used as an indicator for the degree of homogeneity of the material, this suggests a higher number of defects near the GaN substrate.

An interesting observable feature is the Raman frequency change. The frequency of the E$_2$(high) mode changes slightly around the position of maximal FWHM. Tending towards smaller frequencies and subsequently returning to the starting values (fig 10a).
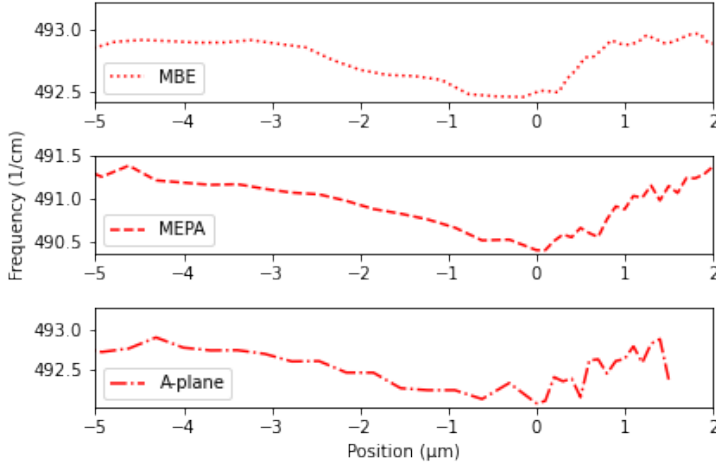

Figure 10: Raman frequencies of the InN E$_2$(high) mode for the MBE a), MEPA b) and A-plane c) sample in relation to the corrected depth of the focus.

The shift towards lower frequencies can be attributed to the lattice mismatch between GaN and InN, as well as to the difference in the thermal expansion coefficient during growth[19] (see table 3). This could also add to the noticeable FWHM behavior.

The lattice mismatch and thermal expansion coefficient create a stress inside the InN at the substrate interface. This compresses/stretches the crystal structure and with it changes the phonon frequency. Under tensile stress, the frequencies are shifted towards lower values. Compressive stress shifts them towards higher frequencies[16, 45, 46]. In conclusion, the observable shift, from higher towards smaller frequencies, indicates a stress relaxation. In other words, a decrease of compressive stress.

Since the lattice constant c$_{GaN}$ is smaller than c$_{InN}$, the dimensions of the GaN c-plane are smaller than in the case of InN. This suggests that in order to grow InN on GaN, the InN atomic structure has to be under stress to fit to the structure of GaN. The lattice mismatch between the c-plane InN and c-plane GaN substrate amounts to {0001}$_{InN}$ ∥ {0001}$_{GaN}$ = 11.1%, calculated with the values in table 3. These calculations do not take the different polarization of planes as well as possible in-plane twisting between atomic structures into

account. For a deeper look into these topics for InN, see for example [18, 20].

In conclusion, the InN layer is under compression at the InN/GaN interface and relaxes with increasing thickness. Thus, the air/InN interface should see the lowest amount of stress caused by the GaN. Furthermore, the relaxation in III-nitrides is accompanied by defects. Such structural imperfections could in turn explain the behaviour of the FWHM as an indicator for the degree of homogeneity.

		GaN	InN	sapphire
Lattice Constant	a	3.194	3.532	4.758
	c	5.177	5.667	12.9991
Thermal expansion coefficient	$\frac{\Delta a}{a}$	5.59	~ 4	7.5
	$\frac{\Delta c}{c}$	3.17	~ 3	8.5

Table 3: Lattice constants of GaN, InN and sapphire(Al_2O^3) in Å, thermal expansion coefficient in 10^{-6}K. Values from [21, 47]

Using this interpretation on the increase in frequency at the air/InN interface suggests an incorporation of defects. But other reasons might be possible.

As the Raman frequency changes with internal stress, the latter can be estimated from hydrostatic pressure dependent Raman measurements. This is possible, since the effect of internal compressive stress and external stress on the sample is equivalent. Both compress the atomic structure and causing a Raman frequency shift. In case of InN, the relevant values are the unstressed Raman frequency $\omega_0 = 492.7$ cm^{-1} and the pressure coefficient $\frac{\partial \omega}{\partial P} = 5.07$ cm^{-1} GPa^{-1}[35]. Inserting these in equation 20 yields the stress inside the sample.

Stress values begin in the positive range and change to negative over a depth of about 2 µm, as can be seen in figure 11. Reparaz at al[35] have chosen a positive sign for their externally applied hydrostatic pressure. As such, positive stress in figure 11 is compressive. In conclusion, the sample is under compressive stress at the InN/GaN interface. The stress changes via relaxation to tensile stress at the surface.
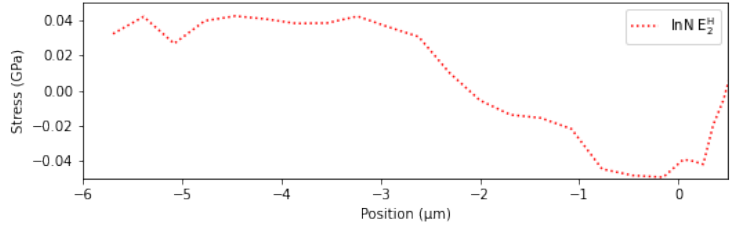

Figure 11: Calculated stress from the E$_2$(high) Raman frequency by applying eq. 20. Positive pressures refers to compression. The used unstressed frequency may not be accurate, resulting in an unknown amount of vertical data shift.

This evaluation should be read with adequate scepticism. Due to the difficulties of creating a InN sample, the used value ω_0 is not accurate as the unstressed E$_2$(high) Raman frequency. The graph is thereby not accurately presenting the actual internal stress.

4.2 InN MEPA

The MEPA sample is a 0.1 μm c-plane InN layer on a-plane sapphire substrate. In back-scattering, the modes E_2(high) and A_1(LO) Modes are expected[21].

Figure 12 shows a representative spectrum. Observed are the E_2(high) at 491 cm^{-1} and LO mode of InN at 590 cm^{-1} as well as visible modes of sapphire(Al_2O_3) at 417, 450, and 749 cm^{-1} respectably. The InN frequencies match well with the reported frequencies by Davydov[41] and Harima[21], see table 2. The modes of sapphire coincide with the ones reported by Porto (418, 451, 751 cm^{-1})[48]. Furthermore, two Skew-normal functions are added to take strongly interacting plasmon-coupled modes into account[39, 43].

Figure 12: Exemplary Raman spectrum of the MEPA sample.

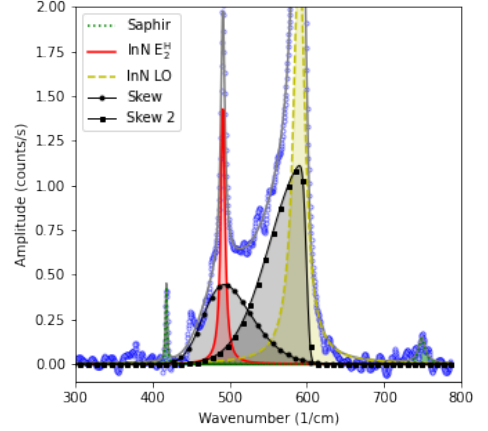All data processing and calculations are identical to the MBE sample, except for the added Skew normal funktion.

The behavior of the InN modes over the depth are depicted in fig 13. The E_2(high) (fig 13b)) and the LO (fig 13c)) modes exibit a similar behavior and have their maximum at -1 μm, with a FWHM of 5 μm for the E_2(high) and 4.8 μm for the LO. Both are broader than the expected layer thickness. Proofing, that the used depth-resolution was to low to resolve the layer.
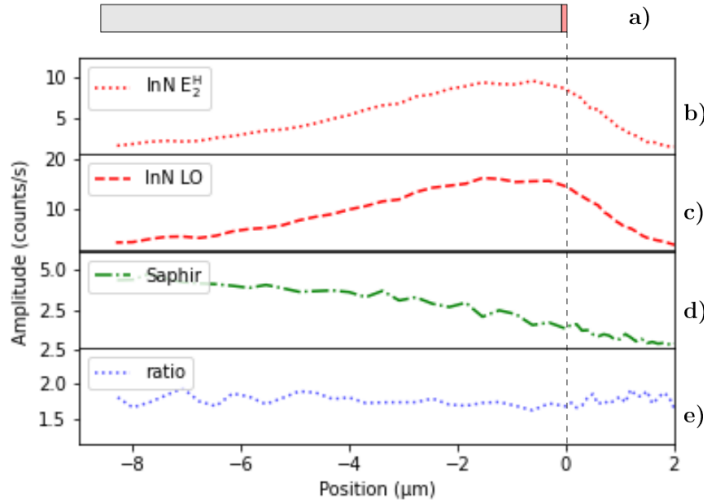

Figure 13: Fitted intensities of the Raman modes plotted in relation to the corrected depth of the focus, with sample structure in (a) as reference for the MEPA sample. InN E_2(high) in (b) and the LO in (c), their ratio in (e). (d) sapphire substrate mode at 417 cm^{-1}.

No overall trend can be noticed in the LO/E_2(high) ratio (fig 13e). This implies a lack of carrier accumulation, but considering the depth resolution this is not meaningful.

The E_2(high) frequency decreases towards the InN/air interface, see fig 10b. Again, this shift can be attributed to the lattice mismatch between the substrate (here a-plane sapphire) and the bulk (c-plane InN), in addition to the difference in the thermal expansion coefficient during growth (see table 3).

The dimensions of the sapphire a-plane are larger than for the InN c-plane. This suggests a tensile stress on the interface. Estimating the lattice mismatch for this configuration is difficult and includes both lattice parameters and a comparison of the areas. As an approximation is the mean of the lattice mismatch for the a and c constants used. The approximated lattice mismatch amounts to $\{0001\}_{InN} \parallel \{11\bar{2}0\}_{sapphire} = -40.6\%$ for one InN c-plane on one sapphire a-plane while for two InN c-planes. Compared to $2 \times \{0001\}_{InN} \parallel \{11\bar{2}0\}_{sapphire} = 18.3\%$. The more likely configuration is therefore the latter, resulting in an compressed structure of InN on the InN/sapphire Interface.

Due to the compressed InN on sapphire, the same argumentation as for the MBE sample applies. The InN is under compression on the interface and relaxes towards the InN/air interface. Do to the tensile character of this change, a shift to lower frequencies is observed.

4.3 InN A-plane

The a-plane sample is a 0.25 µm a-plane InN layer on r-plane sapphire substrate. In back-scattering, the modes E_2 and $A_1(LO)$ Modes are expected[21].

In figure 14 are the E_2(high) at 492 cm^{-1} and E_1(LO) mode of InN at 595 cm^{-1} shown in an representative spectrum. Furthermore, the visible modes of sapphire(Al_2O^3) at 380, 418, 433, 449, and 749 cm^{-1}. The InN frequencies match with the reported frequencies by Davydov[41] and Harima[21], see table 2. The modes of sapphire coincide with the ones reported by Porto[48]. One asymmetric Gaussian function is added to account for strong interacting plasmon-coupled modes[39].
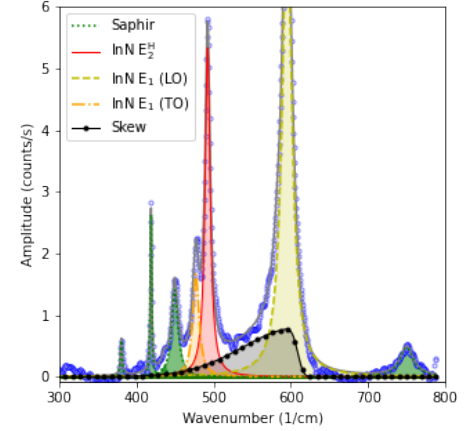

Figure 14: Exemplary Raman spectrum of the A-plane sample.

This sample has an InN thickness comparable to the MEPA sample. Therefore, the depth-resolution is not good enough to accurately display the layer with a confocal scan. Nevertheless, shows the E_2(high)-LO ratio a noticeable increase towards the InN/air interface (fig 15e). This suggests a carrier accumulation at the sample surface.

The frequency shift exhibits a behaviour comparable to the MEPA sample. As such, the conclusion is that the InN to be under compression on the InN/saphire interface, and relaxation towards the surface creates a shift towards lower Raman frequencies.
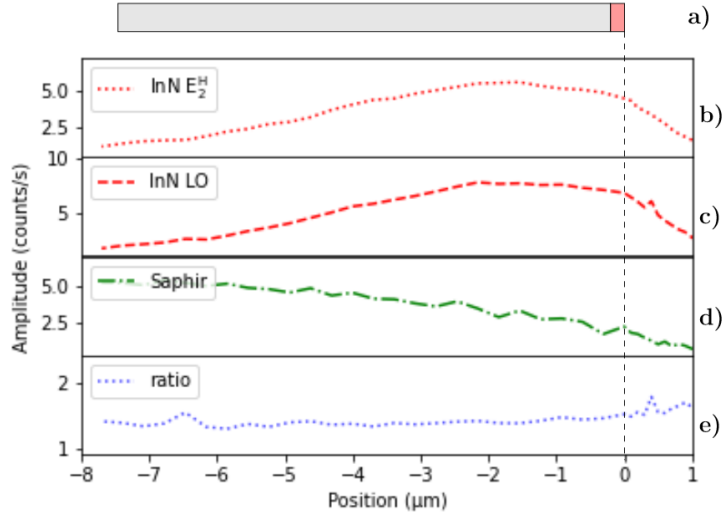

Figure 15: Fitted intensities of the Raman modes plotted in relation to the corrected depth of the focus, with sample structure in (a) as reference for the A-plane sample. InN E_2(high) in (b) and the LO in (c), their ratio in (e). (d) sapphire substrate mode at 418 cm^{-1}.

5   Martin's double resonance

Davidov et al[41, 49] have shown that the frequencies of the phonons $E_1(LO)$ and $A_1(LO)$ shift towards higher frequencies as the exiting radiation energy decreases. The $A_1(TO)$ and the $E_2(high)$ remain unaffected. This is attributed to the Martin's Double Resonance effect[50, 51]. Here an electron-hole-pair is excited by photons with an energy larger than the fundamental band gap into a real state in the conduction band. Consequently, scattered elastically by impurities into another state. From this state the pair scatters inelastic into an intermediate state by interaction with a phonon and from there relaxes to the ground state[50, 51]. By approximating the dispersion of the electronic bands, it is possible to calculate the wavevectors of the electron-hole-pair that is exited by the incoming photons[49, 52]. For this, the expressions

$$\epsilon^e(k) = E_g + E_e \left[\sqrt{\frac{\hbar^2 k^2}{2m_\Gamma^e E_e + \frac{1}{4}}} - \frac{1}{2} \right] \tag{21}$$

$$\epsilon^{lh}(k) = -E_{lh} \left[\sqrt{\frac{\hbar^2 k^2}{2m_\Gamma^{lh} E_{lh} + \frac{1}{4}}} - \frac{1}{2} \right] \tag{22}$$

$$\epsilon^{hh}(k) = -\frac{\hbar^2 k^2}{2m_\Gamma^{hh}} \tag{23}$$

are used[49, 52]. $E_g = 0.63$ eV is the band gap at room temperate, while $E_{e,lh}$ are the non-parabolic parameters for the conduction band and the band of light holes respectively with $E_e = 0.4$ eV and $E_{lh} = 0.8$ eV. Furthermore, $m_\Gamma^{e,lh,hh}$ are the effective masses of electrons, light holes and heavy holes at the Γ-point with values of $m_\Gamma^e = 0.07 m_0$, $m_\Gamma^{lh} = 0.0035 m_0$ and $m_\Gamma^{hh} = 0.4 m_0$ in units of the electron mass $m_0 = 9.10938 \cdot 10^{-31}$ kg[49]. The bands as well as the dispersion of e-h-pairs, from the difference between the conduction and valence band, are shown in figure 16.
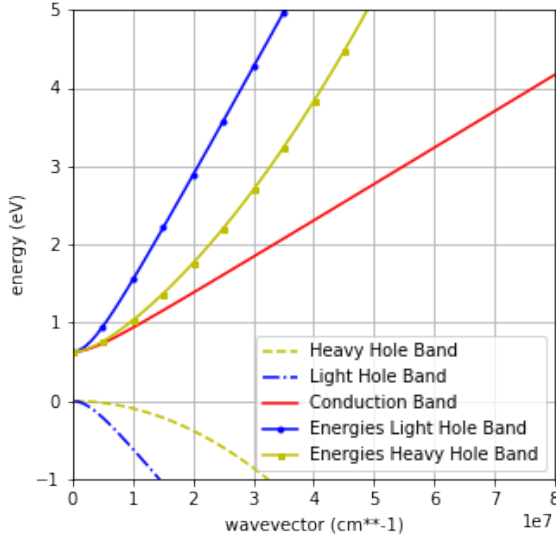

Figure 16: Approximated band dispersion curves for conduction band and light/heavy hole valance band, respectably. Energies between conduction and valance bands from differences.

By calculating the energy of the incoming radiation, it is possible to extract the wave vector k of the radiation from the band dispersion diagrams for the light hole and heavy hole bands. The momentum of phonons that are scattered by the double resonance process is then

$$q = 2 \cdot k \tag{24}$$

in units of cm^{-1}[49].

The Raman spectra are fitted with Gaussian line shape for Landau damping regime and LPP modes, Lorentzian line shape for uncoupled and substrate modes as well as Skew normal functions for plasmon coupled modes[39]. Measured LO Raman frequencies for 266 and 405 nm are plotted as a function of the phonon wavevectors in figure 17, alongside values from, Ries (458 to 830 nm)[39]. The phonon dispersion presented by Davydov at al. [41, 49] is depicted as well.

The measured frequencies should follow the band structure for either the light or heavy holes. But the values acquired by Ries do not suffice to distinguish between Γ-M and Γ-K dispersion direction.

Values for 266 and 405 nm reveal the direction of this process to be along Γ-M for the a-plane and MBE sample.

All values follow the band structure, except for the 266 nm on. InN possesses a single conduction band up to 4 eV[53]. Beyond, is a direct interaction between electron-hole pairs and phonons difficult to assign to single electronic transition.

It is strange that the MBE sample behaves like the a-plane sample, rather than the MEPA c-plane. This could be caused by the etching of the sample, resulting in an enlarged surface area and allowing multiple facets. Another explanation could be that the sample is burnt during laser exposure. Why this would only happen by the MBE and not by the other sample is unknown.
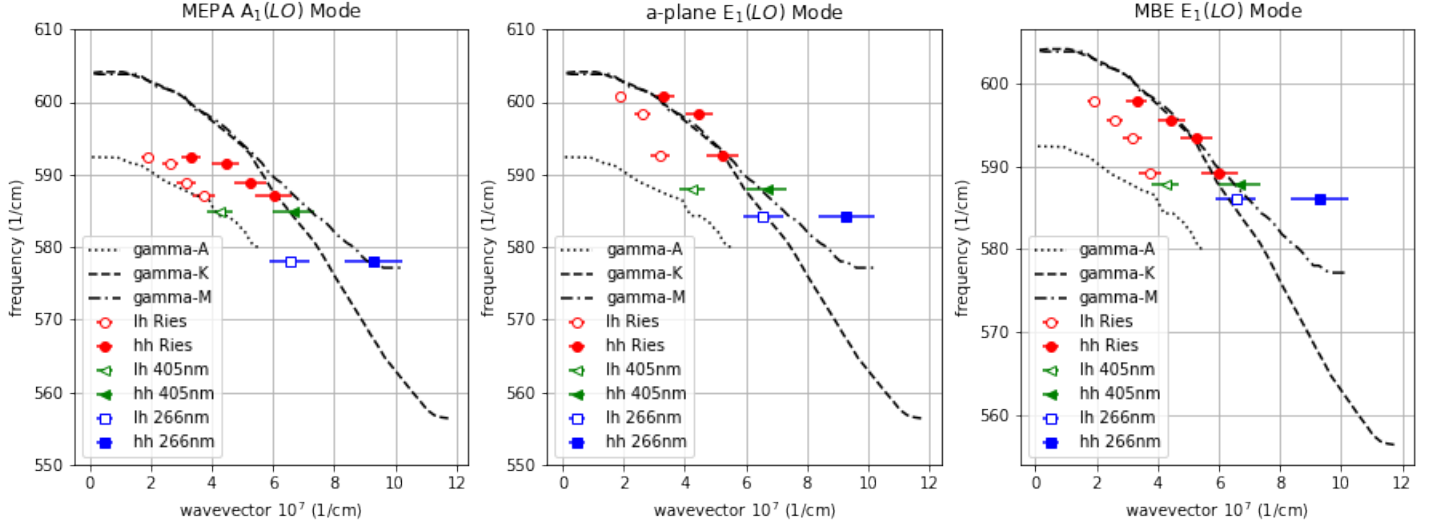

Figure 17: Frequencies of LO modes as a function of the phonon dispersion wave vectors.

6 Depth-resolved Raman spectroscopy of GaN

The same Raman experiments and analysis has been performed for a GaN sample. In this case the best possible resolution was used, i.e. the lowest possible confocal pinhole aperture (in this case 50 µm) with the expected drawback of a prolonged measuring time. Figure 18 depicts a number of intensity depth diagrams from the measurements of the sample with their confocal pinhole apertures in µm.
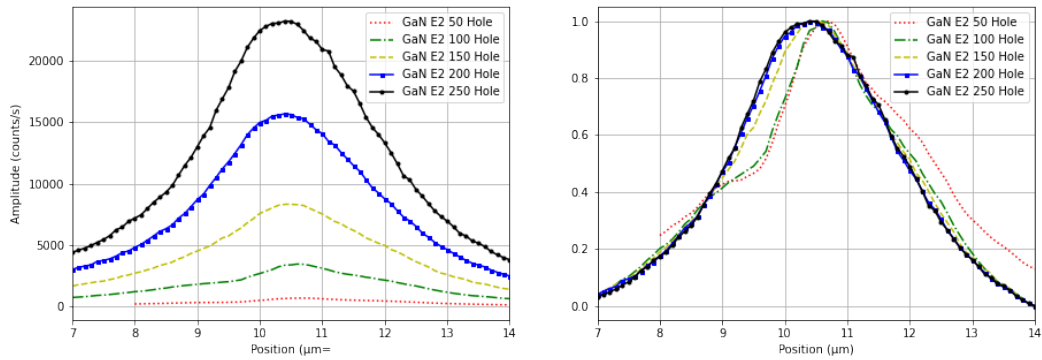

Figure 18: Intensity of the E2 high mode of GaN with varying hole apertures in µm, the smallest confocal pinhole aperture of 50 µm

The E_2(high) frequency shift was used to calculate the stress inside the GaN[35] with values from [54, 55] and is compared with calculated stress from *in situ* curvature measurement. The results will be published as a separate paper and the latest version (by the time of submission of this bachelor thesis) is included below:

Depth-resolved Raman spectroscopy of GaN compared with in situ stress

F. Heisinger,[1, a)] Dr M. Ries,[1] Dr. A. Dadgar,[2, b)] and Dr. M. Wagner[3]

[1)]*Authors' institution and/or address*
[2)]*Second institution and/or address*
[3)]*Institution and/or address*

(*Electronic mail: Second.Author@institution.edu.)

abstract

I. INTRODUCTION

GaN and other nitride based materials are broadly used in detectors, lasers or amplifier due to there respected efficiency and properties. Their growth is carried out by heteroepitaxy procedure that due to lattice and thermal coefficient mismatches tends to produce defects inside the grown layer. Furthermore in situ measurements show a bending of the material as a whole due to differences in the respected material surface energy.

In this work we use a depth resolved confocal Raman microscope, which allows the investigation of layer parameters and study of changes regarding the Raman frequency with depth. Farther can the Raman frequency shifts be used tho argue about the stress inside the sample in question as well as compared with stress emerging by the growth process and noticed by in situ measurements.

II. EXPERIMENTAL METHODS

A. Sample Description

The sample in question is a GaN layer doped with Ge on undoped GaN grown on sapphire substrat by Metalorganic vapour-phase epitaxy (MOVPE). The respected layer thickness includes a 5.1 µm doped GaN layer with Ge, a 2 µm undoped GaN layer, and a buffer containing a SiN mask, a 100 nm AlGaN-gradient, a 200 nm AlN layer and a LT-AlN seed. The overall sample thickness is 0.455 mm.

Hall measurement by the manufacturer showed a carrier concentration of 1.6×10^{20} cm^{-1}.

B. Measurement System

The measurement system uses a 532 nm external laser for a HORIBA HR800 integrated Raman system. A x100 MPlan N objective with an numeric aperture of NA = 0.9 is used in the pre included microscope as well as an edge filter for 532 nm. The measurements are taken in $z(-,-)(\bar{z})$ backscattering geometry.
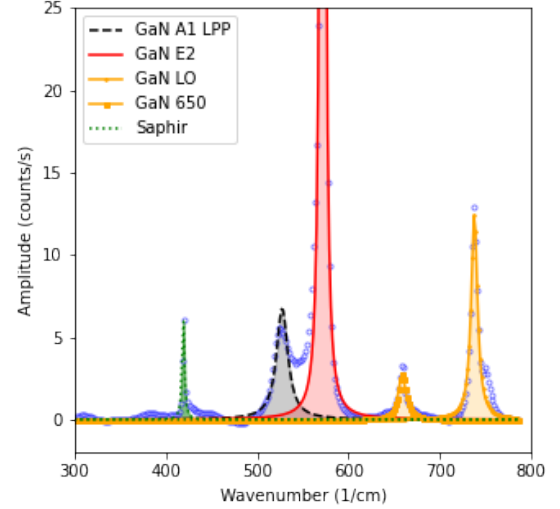
———————

[a)]Also at Physics Department, XYZ University.
[b)]http://www.Second.institution.edu/~Charlie.Author.

Figure 1. Exemplary Raman spectrum of the sample. Fitted are the E$_2$(high), A1 LPP and LO of InN as well as a made at 650 cm^{-1}, and a mode of sapphire at 418 cm^{-1}.

III. EXPERIMENTAL RESULTS AND DISCUSSIONS

A. Focal point shift

Due to the refraction on interfaces the measured distances by the movement if the Z-piezo stage in depth differ from the actual focus position and have to be corrected. Baldwin and Batchelder derived a equation for determining the mean focal depth[1]. Under the assumption of a fractional height of $\frac{r}{r_{max}} = \frac{1}{2}$, and a refraction index for GaN of n= 2.4 the compression factor $\frac{z}{z_0} = 2.8$ is obtained.

B. Depth-dependent Raman spectra

Shown in fig 1 are mainly the E$_2$(high), LO and A1 LPP mode of GaN at 571, 737 and 530 cm^{-1} with another mode of GaN at 658 cm^{-1} as well as sapphire modes found at 418, 645 cm^{-1} respectively in one of the acquired spectra. These frequencies match quite well with the reported frequencies by Davydov[2] and Harima[3] except the ones arround 650 cm^{-1} which could not be fitted accurately because of low intensity.
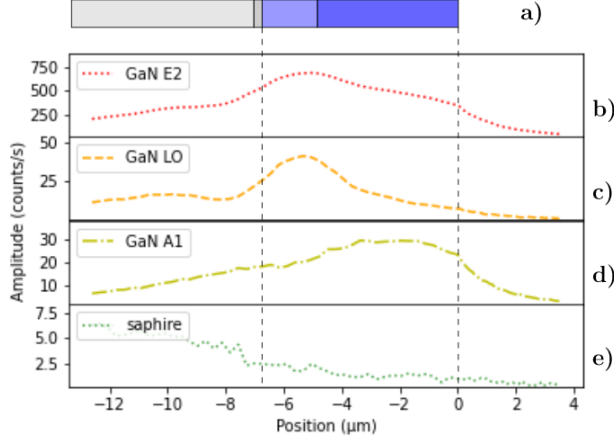
Figure 2. Fitted intensities of the Raman modes plotted in relation to the corrected depth of the focus, with sample structure in a) as reference. E_2(high) in b), the LO in c), and the A1 LPP in d). With a saphhire mode in e).

In figure 2 the changing amplitude of the GaN E_2(high) and LO as well as the A1 LPP mode, that arises from Longitudinal-optical phonon-plasmon (LPP) coupling due to germanium (Ge) doping, is shown. As the lens fokus is moved towards the sample surface (towards a higher position) the intensity of the LO mode rises alongside the E_2(high) mode until it is overtaken by the LPP mode. This suggests the crossing into the Ge doped region of the GaN layer. This is further confirmed by the FWHM of the amplitude behavior, the E_2(high) spanning around 6.1 μm and the A1 LPP around 4.1 μm compared to the all in all 7.1 μm for the GaN and GaN:Ge layers and 5.1 μm for the GaN:Ge layer alone. As the course is not symmetrical and the fitting difficult, an error of 0.6 μm is estimated for the amplitude FWHMs.

The FWHM of the respected raman peak reflects the crystalline quality[4]. As the GaN E_2(high) is visible throughout the GaN and GaN:Ge layer with a small increase in the GaN:Ge layer it can be concluded that the doping resulted in little lattice disturbances.

The FWHM of the A1 LPP mode has a maximum at 10.4 μm (near the E_2(high) amplitude maximum) and decreases towards the amplitude maximum.

in Figure 3 are the listed the Raman mode frequencies over depth.

C. Stress

The E_2(high) mode of GaN does not interact with carriers do to unchanging electrical potentials of the atomic vibration. Do to this, it is feasible to calculate the internal Stress of the GaN layer via this mode. For this, the frequency shift by stress $\frac{\partial \omega}{\partial P} = 3.4 \text{ cm}^{-1}\text{GPa}^{-1}$[5] and the frequency of unstressed GaN $\omega_0 = 567 \text{ cm}^{-1}$[4] are used in the linear expression in equation 1[6]. Where ω_s is the measured raman frequency and P the
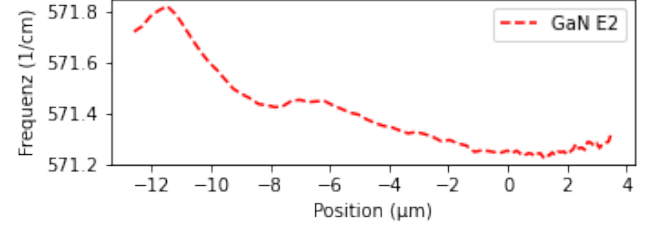

Figure 3. Raman frequency of the E_2(high) mode in relation to the corrected respected depth of the focus.

stress.

$$\omega_s = \omega_0 + \frac{\partial \omega}{\partial P} P \qquad (1)$$

The resulting stress P is shown in figure 4 for the respected depth.

D. In situ data

In situ curvature data from sample growth is used as a comparison for the Raman stress calculation. To use the data, it is necessary to change the growth time x axis into a layer thickness one for the GaN. In situ reflectometrie data of a 633 nm laser is used for this.

The thickness of the GaN, GaN:Ge layer is calculated by the number of oscillations and the time these take on average, from the reflectometrie data. Every oscillation amounts to approx 132 nm of accumulated material, resulting in an average growth of 43.35 nm/min. Form this the relevant data can be expressed dependent in μm scale. The GaN and GaN:Ge layer thickness together, is found to be arround ≈ 8 μm. Further modification of the data is the change of the axis zero in curvature and layer thickness to be at the GaN layer growth start.

Assuming isotropic elastic behaviour and a spatially uniform biaxial mismatch strain ε_m while the substrate is significantly bigger than the film, the Stoney Equation is[7]:

$$\kappa = \frac{6m\varepsilon_m h_f}{h_s^2} \qquad m = \frac{M_f}{M_s} \qquad (2)$$

For the curvature κ and the thicknesses of film and substrate $h_{f,s}$. $M_{f,s}$ is the biaxial moduli calculated from the Young module E and the Poisson Ratio ν via $M = \frac{E}{1-\nu}$. In this situation the relation between the strain ε and the stress σ is $\sigma_f = M_f \varepsilon_m$[7].
The stress is then given by[7]:

$$\sigma_f = \frac{M_s h_s^2 \kappa}{6 h_f} \qquad (3)$$

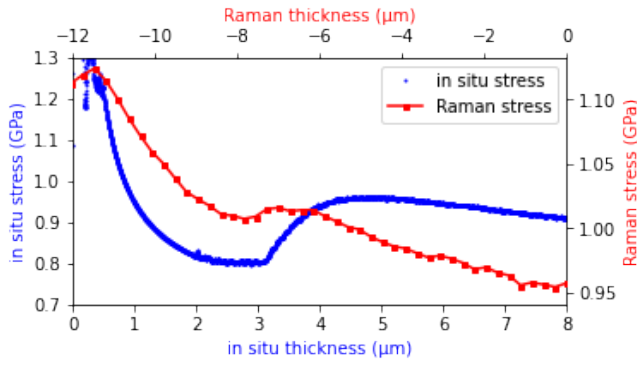κ is the thickness dependent curvature and h_f the changing layer thickness.

Figure 4. Comparison of the stress from Raman frequency shifts and in situ curvature data.

Used values are $M_s = 430.14$ GPa from $E_s = 314$ GPa and $v_s = 0.27$[8] as well as $h_s = 0.4479$ mm. The result is shown in figure 4 compared to the calculated stress from the measured Raman frequency shifts of the GaN E_2(high) mode.

By comparing the stress in figure 4 it can be seen that the stress follows a similar behavior with the thickness. The difference in stress value can be traced back to the used approximation that presupposes total relaxation which stretches the overall trend towards zero. The differences in thickness arrive from the not optimal assumed fractional height and inaccuracies considering the surface point for the stress from the Raman measurements, as well as inaccuracies from the thickness calculation of the in situ curvature data. This shows that there is still stress in the sample structure and that it is highest at the interfaces as well as that the origin is the growth process.

IV. CONCLUSION

V. ACKNOWLEDGEMENTS

REFERENCES

[1] K. J. Baldwin and D. N. Batchelder, "Confocal raman microspectroscopy through a planar interface," Appl. Spectrosc. **55**, 517–524 (2001).

[2] V. Y. Davydov, A. A. Klochikkin, A. Smirnov, and I. Y. Strahkova, "Selective excitation of e_1(lo) and a_1 phonons with large wave vectors in the raman spectra of hexagonal inn," Physical Review B **80** (2009), 10.1103/PhysRevB.80.081204.

[3] H. Harima, "Properties of gan and related compounds studied by means of raman scattering," Journal of Physics: Condensed Matter **14** (2002), https://doi.org/10.1088/0953-8984/14/38/201.

[4] M. Kuball, "Raman spectroscopy of gan, algan and aln for process and growth monitoring/control," SURFACE AND INTERFACE ANALYSIS **31**, 987—999 (2001).

[5] I. Ahmad, M. Holtz, N. N. Faleev, and H. Temkin, "Dependence of the stress–temperature coefficient on dislocation density in epitaxial gan grown on -al2o3 and 6h–sic substrates," Journal of Applied Physics **95**, 1692–1697 (2004), https://doi.org/10.1063/1.1637707.

[6] J. S. Reparaz, K. P. da Silva, A. H. Romero, J. Serrano, M. R. Wagner, G. Callsen, S. J. Choi, J. S. Speck, and A. R. Goñi, "Comparative study of the pressure dependence of optical-phonon transverse-effective charges and linewidths in wurtzite inn," Phys. Rev. B **98**, 165204 (2018).

[7] A. Krost, A. Dadgar, G. Strassburger, and R. Clos, "Gan-based epitaxy on silicon: stress measurements," physica status solidi (a) **200**, 26–35 (2003), https://onlinelibrary.wiley.com/doi/pdf/10.1002/pssa.200303428.

[8] L. M. D. . Commercialization and A. Materials, "Alumina - aluminium oxide - al2o3 - a refractory ceramic oxide," (2001).

7 Conclusion

Depth-resolved confocal Raman spectroscopy has been shown to deliver agreeable results matching theoretical values. However, it strongly depends on the layer thickness with a critical value for the sample thickness being equal to the depth resolution. The MBE sample, having the thickest InN layer, shows layer thickness from the amplitude behaviour of the Raman modes as well as Raman frequency shifts in agreement with theoretical layer thickness and lattice mismatch. The MEPA and a-plane samples on the other hand, due to their small InN layer thickness, can not be evaluated to the same extend. For the minimal possible objective step size of 100 nm only one or two Raman spectra originate from the InN layer. A smaller step size and confocal pinhole could show better results. A slightly better lateral resolution could be achieved by scanning the samples from the side, but would still not be enough for the MEPA and a-plane samples. TERS could be an alternative to survey depth dependent effects in thin layers.

The calculation of the stress inside the sample via the Raman frequency shifts resembles the stress from the *in situ* curvature measurement. But, for accurate calculations, the unstressed parameters and pressure coefficients have to be known. For materials that can not be produced without a substrate, this method can only provide quantitative arguments for the change in stress by thickness.

The depth re-scaling, via the equations of Baldwin and Batchelder, creates agreeable thicknesses. However, the fractional height m should not be assumed, but calculated by the covered area of the objective by the laser beam. This would result in an even more accurate depth distance correction.

The main reason for this work, search for evidence of carrier accumulation via comparison of polar and nonpolar Raman mode (A1(LO) and E_2(high)) due to their different interaction with said carriers, has not delivered definitive results. As the layer thickness of the MEPA and a-plane samples is to small too acquire well-resolved depth-profiles, it is not possible to draw convincing arguments for or ageinst carrier accumulation. For the MBE sample, a carrier accumulation can be assumed via the ratio of the modes. However, the change in ratio is too small to use it as a definitive argument. Probably, by increasing the resolution of the Raman spectra on the spectral area in question and improve the accuracy of the fitting functions for the respective data could enhance the understanding.

References

[1] Jacob Millman and Christos C. Halkias. *Millman's Integrated Electronics*. MC GRAW HILL INDIA, 2009. ISBN: 9780070151420.

[2] Jinmin Li and G. Q. Zhang. *Light-Emitting Diodes: Materials, Processes, Devices and Applications*. Springer, 2019. ISBN: 978-3-319-99210-5. URL: https://doi.org/10.1007/978-3-319-99211-2.

[3] Chenming Hu. *Modern Semiconductor Devices for Integrated Circuits*. PEARSON INDIA, 2009. ISBN: 8131730247.

[4] Russell S. Ohl. "light-sensitive electric device including silicon". U.S. pat. 2,443,542. June 15, 1948. URL: https://patentimages.storage.googleapis.com/21/a3/d9/a1e314a0faba89/US2443542.pdf.

[5] T. Wu. "Mini-LED and Micro-LED: Promising Candidates for the Next Generation Display Technology". In: *Applied Sciences* 8.9 (2018), p. 1557. DOI: 10.3390/app8091557.

[6] I. Akasaki. "Photoluminescence of Mg-doped p-type GaN and electroluminescence of GaN p-n junction LED". In: *Journal of Luminescence* 48-49 (1991), pp. 666–670. DOI: 10.1016/0022-2313(91)90215-h.

[7] T. Nishida, H. Saito, and N. Kobayashi. "Efficient and high-power AlGaN-based ultraviolet light-emitting diode grown on bulk GaN". In: *Applied Physics Letters* 79 (2001), pp. 711–712. DOI: 10.1063/1.1390485.

[8] S. Nakamura, M. Senoh, and T. Mukai. "High-power InGaN/GaN doubleheterostructure violet light emitting diodes". In: *Applied Physics Letters* 62 (19 1993), pp. 2390–2392. DOI: 10.1063/1.109374.

[9] Simon M. Sze and Ming-Kwei Lee. *Semiconductor Devices: Physics and Technology, 3rd Edition*. John Wiley Sons, 2012. ISBN: 978-0-470-53794-7.

[10] Adel S. Sedra and Kenneth C. Smith. *Microelectronic Circuits (The Oxford Series in Electrical and Computer Engineering)*. OXFORD UNIV PR, 2014. ISBN: 9780199339136.

[11] Shuji Nakamura and Shigefusa F. Chichibu. *Introduction to Nitride Semiconductor Blue Lasers and Light Emitting Diodes*. CRC Press, 2000. ISBN: 9780748408368.

[12] Rudolf Gross and Achim Marx. *Festkörperphysik (German) [Solid state physics]*. De Gruyter Oldenbourg, 2014. ISBN: 9783110358704. DOI: doi:10.1524/9783110358704. URL: https://doi.org/10.1524/9783110358704.

[13] Chenming Hu and Richard M. White. *SOLAR CELLS From Basics to Advanced Systems*. McGraw-Hill Book Company, 1983. ISBN: 0070307458. URL: https://www.chu.berkeley.edu/solar-cells-from-basics-to-advanced-systems/.

[14] R H Bube. "Materials for Photovoltaics". In: *Annual Review of Materials Science* 20.1 (1990), pp. 19–50. DOI: 10.1146/annurev.ms.20.080190.000315. URL: https://doi.org/10.1146/annurev.ms.20.080190.000315.

[15] José Antonio Luceño-Sánchez, Ana María Díez-Pascual, and Rafael Peña Capilla. "Materials for Photovoltaics: State of Art and Recent Developments". In: *International Journal of Molecular Sciences* 20.4 (2019). ISSN: 1422-0067. DOI: 10.3390/ijms20040976. URL: https://www.mdpi.com/1422-0067/20/4/976.

[16] Christian Röder. "Strain, charge carriers, and phonon polaritons in wurtzite GaN - a Raman spectroscopical view". PhD thesis. Technische Universität Bergakademie Freiberg, 2014.

[17] Hadis Morkoç. *Handbook of Nitride Semiconductors and Devices, Volume 1, Materials Properties, Physics and Growth*. Wiley, 2009. ISBN: 978-3-527-62846-9.

[18] Duc V. Dinh. "MOVPE growth of InN and InGaN with different surface orientations". Dissertation. Technischen Universität Berlin, 2012. URL: https://www.semanticscholar.org/paper/MOVPE-growth-of-InN-and-InGaN-with-different-Dinh/b36cfdb11296523007b9f7fc679991f24b403d61.

[19] Y. F. Ng et al. "Growth mode and strain evolution during InN growth on GaN(0001) by molecular-beam epitaxy". In: *Applied Physics Letters* 81 (2002). DOI: 10.1063/1.1523638. URL: http://dx.doi.org/10.1063/1.1523638.

[20] A. O. Ajagunna et al. "Epitaxial growth, electrical and optical properties of a-plane InN on r-plane sapphire". In: *Journal of Applied Physics* 107.2 (2010), p. 024506. DOI: 10.1063/1.3284086. eprint: https://doi.org/10.1063/1.3284086. URL: https://doi.org/10.1063/1.3284086.

[21] Hiroshi Harima. "Properties of GaN and related compounds studied by means of Raman scattering". In: *Journal of Physics: Condensed Matter* 14.38 (2002). DOI: https://doi.org/10.1088/0953-8984/14/38/201.

[22] Manuel Cardona Peter YU. *Fundamentals of Semiconductors*. Springer, 2010. ISBN: 978-3-642-00710-1.

[23] NobelPrize.org. *The Nobel Prize in Physics 1930*. URL: https://www.nobelprize.org/prizes/physics/1930/summary/ (visited on 12/01/2021).

[24] Chandrasekhara Venkata Raman. "A new radiation". In: *Indian Journal of physics* 2 (1928), pp. 387–398.

[25] C. V. Raman, F.R.S., and K. S. Krishnan. "A new class of spectra due to secondary radiation". In: *Indian Journal of Physics* 2 (1928), pp. 399–419.

[26] Wolfgang Richter Günther Bauer. *Optical Characterization of Epitaxial Semiconductor Layers*. Springer Verlag Berlin Heidelberg, 1996. ISBN: 978-3-642-79678-4.

[27] horiba.com. *The meaning of confocal Raman microscopy?* URL: `https://www.horiba.com/en_en/raman-imaging-and-spectroscopy-confocal-microscopy/` (visited on 12/06/2021).

[28] edinst.com. *What is Confocal Raman Microscopy?* URL: `https://www.edinst.com/blog/what-is-confocal-raman-microscopy/` (visited on 12/06/2021).

[29] Gurram Giridhar, R.R.K.N. Manepalli, and Gudimamilla Apparao. *ConfocalRamanSpectroscopy*. Ed. by Sabu Thomas et al. Elsevier, 2017, pp. 141–161. DOI: `10.1016/B978-0-323-46140-5.00007-8`. URL: `https://doi.org/10.1016/B978-0-323-46140-5.00007-8`.

[30] Wei Chen et al. "Depth-resolved confocal micro-Raman spectroscopy for characterizing GaN-based light emitting diode structures". In: *The Review of scientific instruments* 84 (Nov. 2013). DOI: `10.1063/1.4829627`.

[31] K. J. Baldwin and D. N. Batchelder. "Confocal Raman Microspectroscopy through a Planar Interface". In: *Appl. Spectrosc.* 55.5 (May 2001), pp. 517–524. URL: `http://www.osapublishing.org/as/abstract.cfm?URI=as-55-5-517`.

[32] A. Krost et al. "GaN-based epitaxy on silicon: stress measurements". In: *physica status solidi (a)* 200.1 (2003), pp. 26–35. DOI: `https://doi.org/10.1002/pssa.200303428`. eprint: `https://onlinelibrary.wiley.com/doi/pdf/10.1002/pssa.200303428`. URL: `https://onlinelibrary.wiley.com/doi/abs/10.1002/pssa.200303428`.

[33] George Gerald Stoney. "The Tension of Metallic Films Deposited by Electrolysis". In: *Proceedings of The Royal Society A: Mathematical, Physical and Engineering Sciences* 82 (1909), pp. 172–175. DOI: `10.1098/rspa.1909.0021`. URL: `https://royalsocietypublishing.org/doi/pdf/10.1098/rspa.1909.0021`.

[34] V. Yu. Davydov et al. "Raman and photoluminescence studies of biaxial strain in GaN epitaxial layers grown on 6H–SiC". In: *Journal of Applied Physics* 82.10 (1997), pp. 161–170. DOI: `10.1063/1.366310`.

[35] J. S. Reparaz et al. "Comparative study of the pressure dependence of optical-phonon transverse-effective charges and linewidths in wurtzite InN". In: *Phys. Rev. B* 98 (16 Oct. 2018), p. 165204. DOI: `10.1103/PhysRevB.98.165204`. URL: `https://link.aps.org/doi/10.1103/PhysRevB.98.165204`.

[36] Timothy David Veal, Christopher F. McConville, and William J. Schaff. *Indium Nitride and Related Alloys*. CRC Press, 2017. ISBN: 9781138116726.

[37] D. Seidlitz et al. "Nanoscale InN clusters and compositional inhomogeneities in InGaN epitaxial layers quantified by tip-enhanced Raman scattering". In: *Applied Physics Letters* 118.16 (2021), p. 162107. DOI: `10.1063/5.0040760`. eprint: `https://doi.org/10.1063/5.0040760`. URL: `https://doi.org/10.1063/5.0040760`.

[38] Emanuele Poliani et al. "Strong Near-Field Light–Matter Interaction in Plasmon-Resonant Tip-Enhanced Raman Scattering in Indium Nitride". In: *The Journal of Physical Chemistry C* 124.51 (2020), pp. 28178–28185. DOI: `10.1021/acs.jpcc.0c04549`. eprint: `https://doi.org/10.1021/acs.jpcc.0c04549`. URL: `https://doi.org/10.1021/acs.jpcc.0c04549`.

[39] Maximilian Daniel Cedric Ries. "Optical analysis of InN and InGaN nanostructures". Doctoral Thesis. Berlin: Technische Universität Berlin, 2021. DOI: `10.14279/depositonce-11647`. URL: `http://dx.doi.org/10.14279/depositonce-11647`.

[40] Gerhard Abstreiter, Manuel Cardona, and Aron Pinczuk. "Light scattering by free carrier excitations in semiconductors". In: *Light Scattering in Solids IV: Electronics Scattering, Spin Effects, SERS, and Morphic Effects*. Ed. by Manuel Cardona and Gernot Güntherodt. Berlin, Heidelberg: Springer Berlin Heidelberg, 1984, pp. 5–150. ISBN: 978-3-540-39522-5. DOI: `10.1007/3-540-11942-6_20`. URL: `https://doi.org/10.1007/3-540-11942-6_20`.

[41] V. Yu. Davydov et al. "Selective excitation of $E_1(LO)$ and A_1 phonons with large wave vectors in the Raman spectra of hexagonal InN". In: *Physical Review B* 80 (2009). DOI: `10.1103/PhysRevB.80.081204`.

[42] Aleksandra B. Djurišić and E. Herbert Li. "Modeling the optical constants of hexagonal GaN, InN, and AlN". In: *Journal of Applied Physics* 85 (5 1999). DOI: `10.1063/1.369604`. URL: `https://aip.scitation.org/doi/abs/10.1063/1.369604`.

[43] S. Buchner and E. Burstein. "Raman Scattering by Wave-Vector-Dependent LOPhonon-Plasmon Modes in w-InAs". In: *PHYSICAL REVIEW LETTERS* 33.15 (1974), pp. 908–911.

[44] A. Pinczuk and E. Burstein. "Fundamentals of Inelastic Light Scattering in Semiconductors and Insulators". In: *Light Scattering in Solids*. Ed. by Manuel Cardona. Berlin, Heidelberg: Springer Berlin Heidelberg, 1975, pp. 23–78. ISBN: 978-3-540-37568-5. DOI: `10.1007/978-3-540-37568-5_2`. URL: `https://doi.org/10.1007/978-3-540-37568-5_2`.

[45] R. J. Briggs and A. K. Ramdas. "Piezospectroscopic study of the Raman spectrum of cadmium sulfide". In: *Phys. Rev. B* 13 (12 June 1976), pp. 5518–5529. DOI: `10.1103/PhysRevB.13.5518`. URL: `https://link.aps.org/doi/10.1103/PhysRevB.13.5518`.

[46] Julián David Correa and Miguel Eduardo Mora-Ramos. *The infuence of compressive lattice deformations on the zone-center energy band properties of zincblende GaN and InN. Hybrid density functional results*. 2021. arXiv: `2108.07381 [cond-mat.mtrl-sci]`.

[47] E.C.F. da Silva et al. "Numerical Data and Functional Relationships in Science and Technology: New Data and Updates for IV-IV, III-V, II-VI, I-VII Compounds, their Mixed Crystals and Diluted Magnetic Semiconductors". In: *Landolt-Börnstein Semiconductors*. Ed. by U. Rössler. Vol. 44 D. Springer Berlin Heidelberg, 2011. ISBN: 978-3-642-14147-8.

[48] S. P. S. Porto and R. S. Krishnan. "Raman Effect of Corundum". In: *The Journal of Chemical Physics* 47 (3 1967), pp. 1009–1012. DOI: `10.1063/1.1711980`. URL: `https://doi.org/10.1063/1.1711980`.

[49] V. Yu. Davydov et al. "Resonant Raman Scattering and Dispersion of Polar Optical and Acoustic Phonons in Hexagonal InN". In: *Semiconductors* 44.2 (2010), pp. 161–170. DOI: `10.1134/S1063782610020065`.

[50] R. M. Martin and T. C. Damen. "Breakdown of Selection Rules in Resonance Raman Scattering". In: *Physical Review Letters* 26.2 (1971). DOI: `https://doi.org/10.1103/PhysRevLett.26.86`.

[51] R. M. Martin. "Resonance Raman sscattering near critical points". In: *Physical Review B* 10.6 (1974). DOI: `https://doi.org/10.1103/PhysRevB.10.2620`.

[52] A. A. Klochikkin et al. "Classical and quatum solutions of the planar accumulation layer problem within the parabilic effective-mass approximation". In: *Physical Review B* 76 (2007). DOI: `10.1103/PhysRevB.97.235325`.

[53] Munise Rakel et al. "GaN and InN conduction-band states studied by ellipsometry". In: *Phys. Rev. B* 77 (11 Mar. 2008), p. 115120. DOI: `10.1103/PhysRevB.77.115120`. URL: `https://link.aps.org/doi/10.1103/PhysRevB.77.115120`.

[54] I. Ahmad et al. "Dependence of the stress–temperature coefficient on dislocation density in epitaxial GaN grown on -Al2O3 and 6H–SiC substrates". In: *Journal of Applied Physics* 95.4 (2004), pp. 1692–1697. DOI: `10.1063/1.1637707`. eprint: `https://doi.org/10.1063/1.1637707`. URL: `https://doi.org/10.1063/1.1637707`.

[55] M. Kuball. "Raman spectroscopy of GaN, AlGaN and AlN for process and growth monitoring/control". In: *SURFACE AND INTERFACE ANALYSIS* 31.10 (2001), pp. 987–999. DOI: `https://doi.org/10.1002/sia.1134`.

Attachment

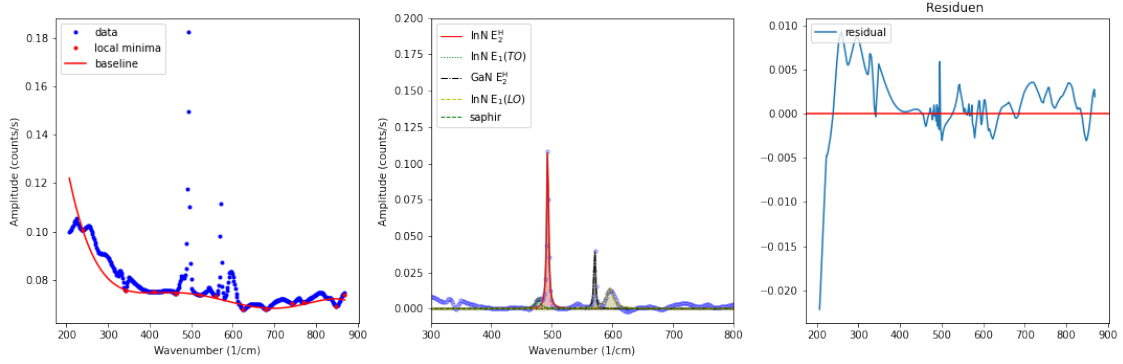## InN MBE fitting change with depth
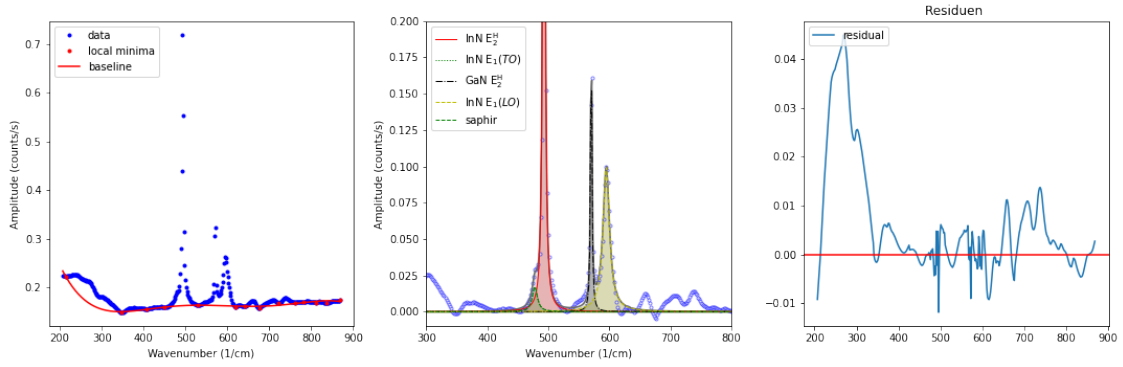

Figure 19: MBE fitting position 5
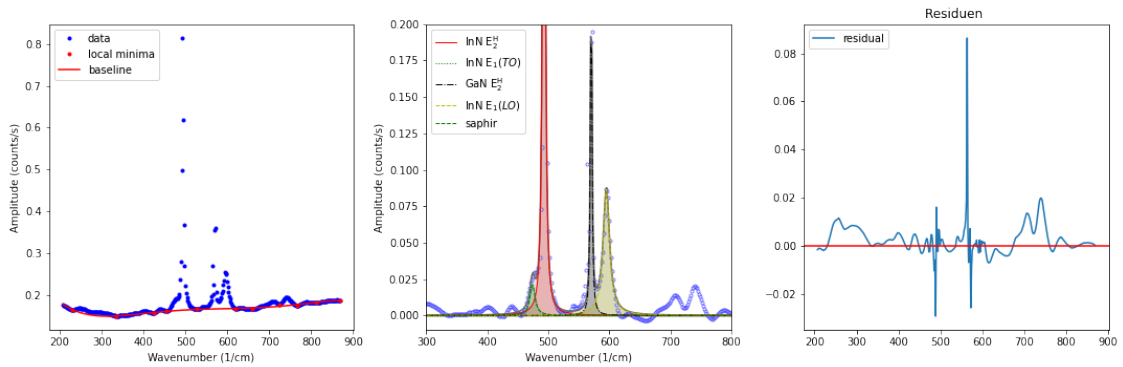

Figure 20: MBE fitting position 1
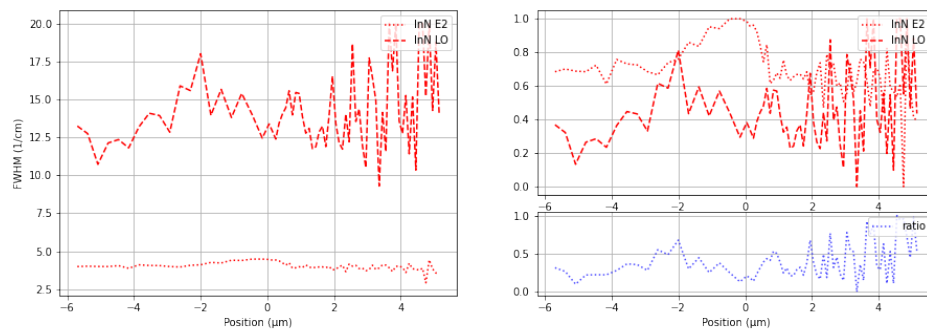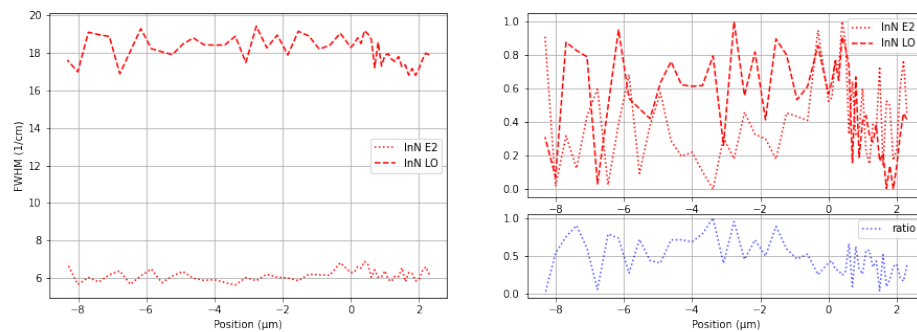

Figure 21: MBE fitting position -5
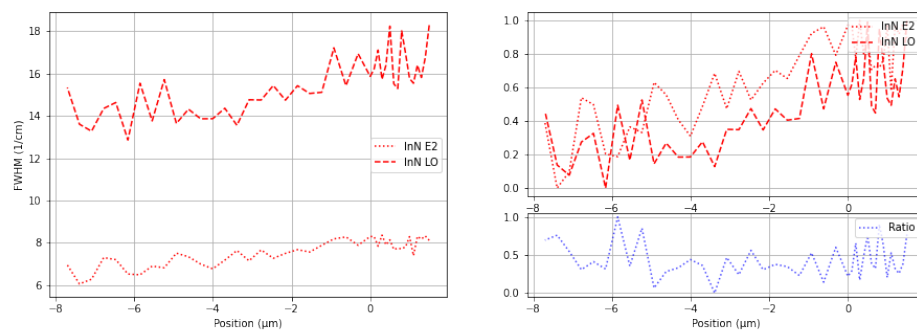
InN FWHM

Figure 22: FWHM MBE

Figure 23: FWHM MEPA

Figure 24: FWHM A-Plane